

# Probing the rheology of continental faults: decade of post-seismic InSAR time-series following the 1997 Manyi (Tibet) earthquake

Minxuan Feng,<sup>1</sup> Lidong Bie<sup>1</sup> and Andreas Rietbrock<sup>1,2</sup>

<sup>1</sup>*School of Environmental Sciences, University of Liverpool, Liverpool L69 3GP, UK. E-mail: fmxorange@gmail.com; L.bie@liv.ac.uk*

<sup>2</sup>*Geophysical Institute, Karlsruhe Institute of Technology, 76187 Karlsruhe, Germany*

Accepted 2018 July 20. Received 2018 June 27; in original form 2017 November 27

## SUMMARY

The physical processes driving post-seismic deformation after large earthquakes are still debated. As in most cases relatively short observation time periods are being used, it is still challenging to distinguish between the different proposed mechanisms and therefore a longer observation time is needed. The 1997  $M_W$  7.6 Manyi, Tibet, earthquake has an excellent InSAR data archive available to study the post-seismic deformation up to  $\sim 13$  yr after the earthquake. The coseismic and early post-seismic phases of the Manyi earthquake were already investigated in detail by numerous studies with viscoelastic and afterslip models being used to explain the post-seismic deformation. We use SAR (Synthetic Aperture Radar) data obtained from the ERS and Envisat satellites covering the central part of the Manyi fault from 1997 to 2010 to significantly extend the observation period. We test different viscoelastic (uniform Maxwell, Standard linear solid and Burgers body rheology below an uppermost elastic layer) and afterslip models to assess the most suitable mechanism for post-seismic deformation. While a Maxwell rheology (misfit = 2.23 cm) is not able to explain the observed long time-series, the standard linear solid (misfit = 2.07 cm) and Burgers body models (misfit = 2.16 cm) with two relaxation times, cannot reproduce sufficiently the localized deformation patterns. The afterslip model (misfit = 1.77 cm) has the lowest misfit and explains well the temporal and spatial pattern of observed deformation. A combined mechanism model that considers the effects of both afterslip and viscoelastic relaxation is also a feasible process, where the viscoelastic relaxation can slightly improve the fit to the data especially at larger distances from the fault. The maximum average line-of-sight velocity is  $\sim 4$  mm yr<sup>-1</sup> during 2008–2010, suggesting that the post-seismic deformation of the Manyi earthquake might be vanishing and gradually stepping into an interseismic phase.

**Key words:** Fault zone rheology; Radar interferometry; Seismic cycle; Asia; Time-series analysis.

## 1 INTRODUCTION

Various mechanisms are employed to explain post-seismic deformations following large earthquakes, including viscoelastic relaxation (e.g. Pollitz *et al.* 2000), afterslip (e.g. Bürgmann *et al.* 2002) and poroelastic relaxation (e.g. Jonsson *et al.* 2003). On the timescale of several years, viscoelastic and afterslip mechanisms are believed to be dominant processes (Wright *et al.* 2013). A range of rheological models is used to simulate viscoelastic relaxation, such as the Maxwell model (e.g. Ryder *et al.* 2014), the standard linear solid model (e.g. Ryder *et al.* 2007) and the bi-viscous Burgers body model (e.g. Pollitz 2005). There currently exists no single mechanism that can explain all observed deformation after large earthquakes, and this must be evaluated on a case-by-case basis. Even for an individual event, different mechanisms are capable of producing

observed surface displacements independently or in combination. For example, afterslip is the only mechanism to explain the 2004 Parkfield earthquake post-seismic deformation (Freed 2007) while afterslip needs to be combined with a viscoelastic model to explain 2001 Kokoxili earthquake (Wen *et al.* 2012).

Previous studies have mostly focused on a short time span of post-seismic deformation, depending on the geodetic observation capability. Only a small number of studies have explored decade-scale or longer post-seismic deformation (e.g. Nishimura & Thatcher 2003; Suito & Freymueller 2009; Copley 2014; Copley & Reynolds 2014; Ryder *et al.* 2014; Hussain *et al.* 2016). It is widely accepted that post-seismic motion decays over time, therefore longer observational periods of post-seismic deformation can help to distinguish between possible mechanisms. A case study by Pollitz *et al.* (2000) on the Landers earthquake concluded that over 3 yr (short time-

scale) viscoelastic relaxation in the lower crust/upper mantle is the dominant post-seismic process. Over longer time-scales, 7 yr, however, a combination of poroelastic relaxation and localized shear deformation is more suitable to explain geodetic data after the Landers earthquake (Fialko 2004). An alternative is the analysis of 1999 Hector Mine earthquake post-seismic deformation by Pollitz (2015), where the influences of afterslip and viscoelastic relaxation at different timescales are discussed.

The  $M_w$  7.6 Manyi earthquake occurred on 1997 November 8, in north-central Tibet. This is a shallow strike slip event as expressed by the CMT solution from the Harvard catalogue (Dziewonski *et al.* 1981; Ekström *et al.* 2012). The epicentre is located close to Manyi fault (Fig. 1), south of the Chaoyang Lake. Satellite geodesy maps clearly rupture of the Manyi earthquake at the surface, spanning a total length of about 170 km (Peltzer *et al.* 1999; Funning *et al.* 2007). The Manyi fault is a sub-fracture of the Xianshuihe–Ganzi–Yushu fault (e.g. Qidong *et al.* 2010) that lies on the boundary between Bayan Har terrane and Qiangtang terrane (Fig. 1). It is located inside the Rola Kangri suture zone, which is the westward extension of Jinsha suture zone. The rate of interseismic slip of the Manyi fault is  $\sim 3 \pm 2$  mm yr<sup>-1</sup>, as determined by Bell *et al.* (2011), using 5 yr of interferograms before the Manyi event.

Previous studies have documented the early post-seismic phases of Manyi earthquake in detail. Ryder *et al.* (2007) found that standard linear solid model and afterslip model could both be used to describe the post-seismic deformation. Ryder *et al.* (2011) also reanalysed the Manyi post-seismic InSAR data using a Burgers body rheology. Yamasaki & Houseman (2012) proposed a complex Maxwell-type model with depth-dependent viscosity. Hetland & Zhang (2014) pointed out that a model composed of a lower Maxwell viscoelastic region with a shear zone beneath the fault could be an alternative mechanism of the post-seismic deformation. All results (from all aforementioned studies) were based on the same data set, which was compiled by Ryder *et al.* (2007), containing only 4 yr post-seismic deformation measurements following the Manyi earthquake. A more extended time span of post-seismic observation is required to investigate the dominant mechanisms at different timescales.

Satellite geodesy can provide us with a high-resolution description of the post-seismic surface deformation over a time period of more than 12 yr in the Manyi region. Low levels of human activity and vegetation coverage provide an ideal set of conditions for the application of InSAR in the Manyi area. Here, we compile a long timespan InSAR data set covering the central part of the Manyi fault from 1997 to 2010 to analyse time-dependent deformation. Ground deformations are compared with different rheological models to find the best-fitting mechanism. We create rate maps, to estimate the deformation rate and then compare this with the interseismic strain accumulation rate (Bell *et al.* 2011) to assess the current earthquake cycle phase.

## 2 DATA PROCESSING AND TIME-SERIES

SAR data were obtained from ERS-2 and Envisat satellites of European Space Agency, operating at C-band with a wavelength of 5.6 cm. The incidence angle of ERS and Envisat is about 23 deg. We analyse data over a period between 1997 and 2010 that covers almost the entire length of the Manyi fault (Fig. 1). Details of the data processing for each satellite are given in Table 1. Data were processed using open source software ROI.PAC developed by

Caltech/JPL (Rosen *et al.* 2004). One descending track (305) was used. Interferograms were formed by pairs of SAR data of which the baseline is smaller than 200 m. Most interferograms are constructed by four frames (2871, 2889, 2907, and 2925). Topographic effects were removed using a 3 arcsecond posting (90 m) digital elevation model, provided by NASA's Shuttle Radar Topography Mission (Farr *et al.* 2007) and interferograms were flattened before unwrapping.

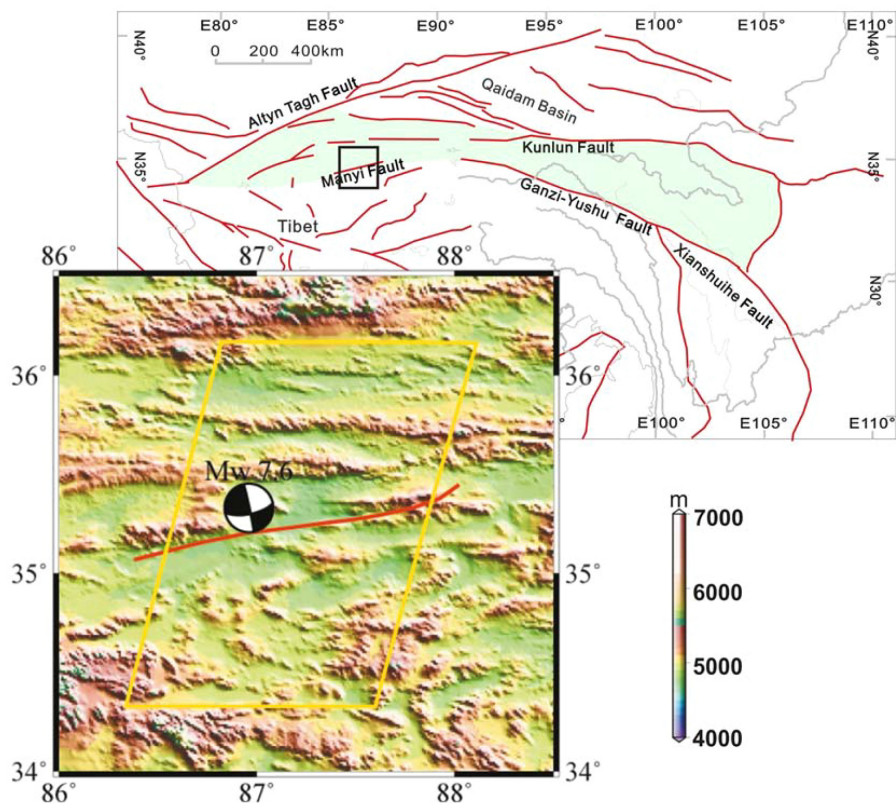
To minimize the errors, topography-correlated tropospheric delays were removed by using a second-order polynomial representation with respect to elevation. This correction approach is based on an empirical linear relationship between the interferometric tropospheric delay and the topography estimated from data obtained from a non-deforming region (Cavalié *et al.* 2007). The constant index is estimated from the non-deformed region and then used to calculate the tropospheric delay for the whole interferogram. Finally, the tropospheric delay is subtracted from the raw interferogram. The insufficient or incorrect orbital ramp also needs to be addressed. In theory, the post-seismic deformation caused by any given earthquake should decay to zero if the location is sufficiently far from the fault. We masked out the deformation area and implemented the far-field deformation close to zero by quadratic corrections. This trend is further subtracted from the whole interferogram. Fig. 2(a) shows the resultant interferogram after all corrections applied reducing the standard deviation from 0.36 to 0.32 cm. The relatively small reduction in standard deviation indicates that the atmospheric noise level of the Manyi area is low, which has been attributed to low vegetation coverage and plateau subfrigid climate (Wright *et al.* 2004; Ryder *et al.* 2007).

As can be seen in Fig. 2(a), the northern lobes show a positive range change, indicating motions away from the satellite. The southern lobes show the opposite, a negative range change. The distinctive boundary change between these two lobes is consistent with the fault trace. Fig. 2(b) shows a cross-section of the topography and the observed post-seismic deformation of the Manyi area along a 0.3 deg-wide swath centred on the profile line for different time steps from early to late. In these profiles, the maximum displacement is at about 10 km away from the fault (Fig. 2b). The line-of-sight (LOS) amplitude is  $\sim 3$  cm during 1997–1998 and decreases to  $\sim 1$  cm during 2005–2008. Finally, the LOS amplitude reduces to  $\sim 0.5$  cm during 2008–2009. A decreasing rate of deformation is observed. Displacements are still measurable even 10 yr after the event. The surface deformations are mainly distributed in close proximity to the fault, indicating a localized deformation pattern.

The InSAR time-series is constructed utilizing the Small Baseline Subset algorithm (Berardino *et al.* 2002) and least-squares inversion (Schmidt & Bürgmann 2003). All images were down-sampled by a factor of 10. Details of the calculation process may be found in Appendix A. Fig. 3 shows the time-series for track 305. A clear and steep displacement gradient across the fault trace is observed and deformation is increasing over time. Moreover, the post-seismic deformation seems to have a localized pattern, as the deformations mainly concentrate at a distance of  $\sim 50$  km from the fault.

## 3 MODELLING

Using our constructed high spatio-temporal geodetic observations (timespan of 12 yr), we explore different proposed mechanisms. Only areas that extend up to 100 km at both sides of the fault (region of significant observable deformation) are used in the modelling to minimize the influence of incoherent noise in the deformation



**Figure 1.** Tectonic map (top right) and location map (left). The green block represents the Bayan Har terrane. The Xianshuihe–Ganzi-Yushu fault is the southern boundary of Bayan Har terrane. Left map shows the location of Manyi fault and Manyi earthquake. The Manyi fault is shown in red. The focal mechanism and epicentral location are taken from the GCMT catalogue. The yellow box shows the area covered by SAR images (Track 305), which were used in this study.

**Table 1.** Details of data used in InSAR time-series analysis.

Track	Geometry	Satellite	Date of First Acquisition yyyy-mm-dd	Date of Last Acquisition yyyy-mm-dd	Number of Dates
305	Descending	ERS	1997-12-02	2001-12-11	7
305	Descending	Envisat	2003-10-07	2010-08-31	29

signal. Coseismic slip parameters are taken from Funning *et al.* (2007). Misfit is calculated from cumulative LOS displacements for all considered pixels.

$$\chi = \sqrt{\frac{1}{n} \left( \sum_{i=1}^n [(d_i - m_i)^2] \right)}, \quad (1)$$

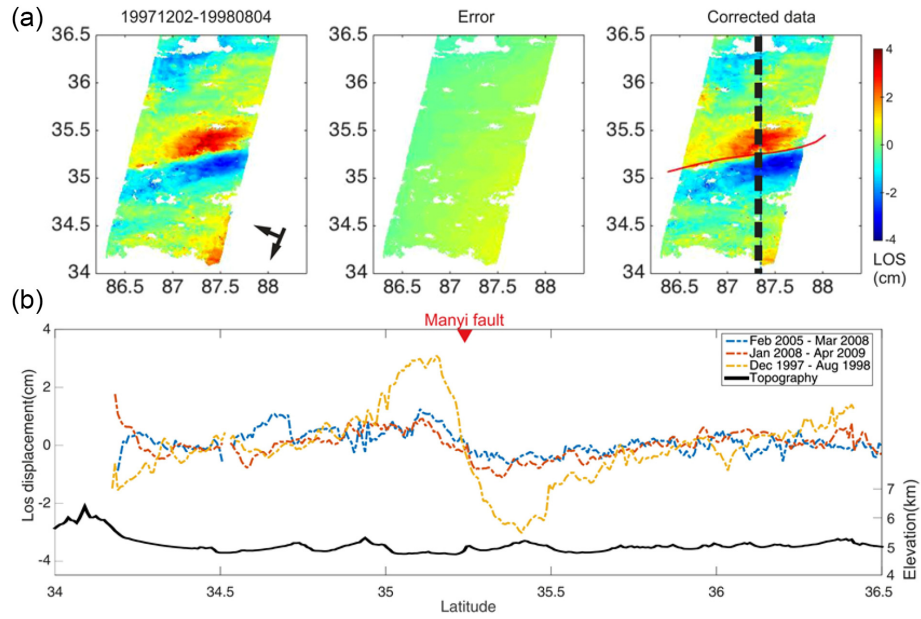
where  $\chi$  is the misfit,  $n$  is the point number in a single image;  $d_i$  and  $m_i$  are the displacement from data and model prediction for the  $i$ th pixel. After the misfit for each date is calculated, we evaluate the overall misfit by averaging the cumulative misfits over time.

### 3.1 Viscoelastic modelling

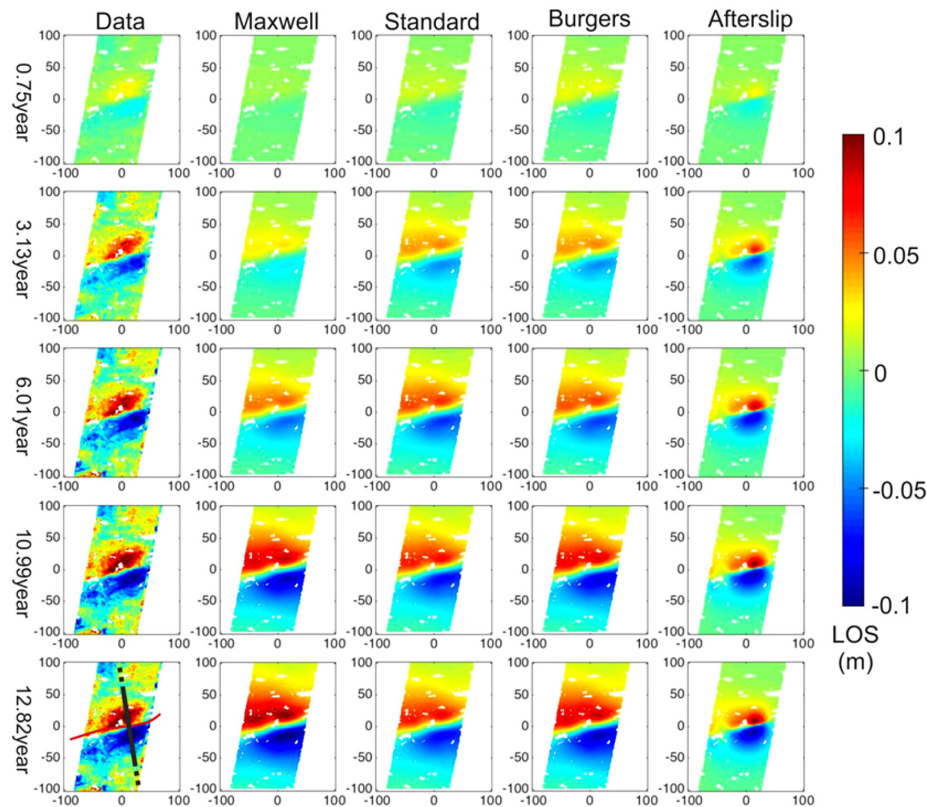
Here we assume that the stress impulse caused by the earthquake will be relaxed by viscous flow within the viscoelastic lower crust. The viscosity controls the stress relaxation time. In this study, we mainly consider three viscoelastic rheologies: the Maxwell, standard linear solid and Burgers body. A schematic configuration depicting different rheologies is shown in Table 2. The elastic spring responds to immediate stress loading, and the damper dominates the steady-state strain rate.

The earth model is constructed using an elastic layer overlying a viscoelastic medium. The crustal thickness is  $65 \pm 5$  km beneath the central Tibet from Magnetotelluric data (Zhao *et al.* 2001). Jiang *et al.* (2006) estimate that the crustal thickness of Bayan Har terrane is on the order of 70 km. Therefore we chose the base of the crust at 70 km for this study. The upper crust thickness varies from 10 to 25 km through the Tibet plateau (Zhao *et al.* 2001). In this study, the elastic layer is fixed to a depth of 15 km as most coseismic slip occurs above this depth (Ryder *et al.* 2007). The rheology of the viscoelastic layer is changed according to different model features. An open-source software package VISCOID (Pollitz 1997) was used to model viscoelastic deformation.

Before modelling the post-seismic deformation, it is helpful to explore the sensitivity of different rheological model parameters on the surface deformation. We run forward calculations for the Maxwell, standard linear solid and Burgers body models while only varying one parameter at a time to examine the effect on the predicted surface deformation. We are most interested in the mean displacements in the observation area and the decay time of the transient phase. We show mean displacement as a function of time since the earthquake. For simplicity, we use the fault geometry


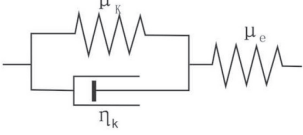
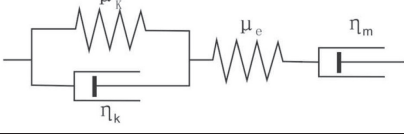



**Figure 2.** (a). An example demonstrating mitigation of atmospheric noise. Panels from left to right show an original interferogram of the Manyi earthquake (19 971 202–19 980 804), estimated error and corrected interferogram. Arrows show the direction of the descending satellite track (SSW) and its corresponding look direction (WNW). Red line is the 11-segment coseismic fault trace as obtained from satellite imagery (Funning *et al.* 2007). The black dash line indicates the profile location for both topography and interferograms in panel (b). (b). Profiles of several interferograms, along with the topography (separated onto two scales for clarity). The red triangle shows the location of Manyi fault.



**Figure 3.** Post-seismic time-series and corresponding best-fitting modelling results. Here, only five dates are presented to show the time-series change tendency. The first column is the time-series from data; the rest columns are the Maxwell, standard linear solids, Burgers and afterslip. The coordinate axis is in kilometre. In the left bottom subplot, the red line indicates the fault trace; the black bold line indicates the profile location in Figs 7 and 10.

**Table 2.** Best-fitting viscosities and misfits for each model.

Model name	Model schematic	Best fit parameters	Misfit (cm)
Maxwell		$\eta=7\times 10^{18}\text{Pa s}$ $\mu_e=3\times 10^{10}\text{Pa}$	2.23
Standard linear solid		$\eta=3\times 10^{18}\text{Pa s}$ $\mu_e=3\times 10^{10}\text{Pa}$ $\mu_k=2\times 10^{10}\text{Pa}$	2.07
Burgers body		$\eta_k=2\times 10^{18}\text{Pa s}$ $\eta_m=1\times 10^{19}\text{Pa s}$ $\mu_e=3\times 10^{10}\text{Pa}$ $\mu_k=6\times 10^{10}\text{Pa}$	2.16
Afterslip		$\mu_e=3\times 10^{10}\text{Pa}$	1.77

of the Manyi earthquake (strike, dip, length etc. from Funning *et al.* 2007) in this parameter sensitivity test.

The Maxwell analogue is composed of a spring with shear modulus  $\mu_e$  and a viscous damper with viscosity  $\eta$  in series (see Table 2) and has a single relaxation time  $\tau = \frac{\eta}{\mu_e}$ . The Burgers body model is represented by a Kelvin element in series with a Maxwell element (see Table 2). This configuration has two relaxation times due to two viscous components. The standard linear solid model is an extreme case of the Burgers body model for which the Maxwell viscosity ( $\eta_m$ ) becomes infinite. When  $\eta_m$  increases to  $1 \times 10^{21}$  Pa s or larger, the Burger modelling results are nearly equal to the standard linear model in our test. The steady-state viscosity  $\eta_m$  controls the magnitude of displacement because the Burgers body model is more sensitive to Maxwell viscosity (Ryder *et al.* 2011). Details of the parameter range explored for each viscoelastic model (shear modulus and viscosity) are given in Appendix B.

In our study, the elastic modulus  $\mu_e$  is assumed at  $3 \times 10^{10}$  Pa and the Maxwell viscosity ( $\eta_m$ ) is taken in the range of  $10^{18}$ – $10^{20}$  Pa s for all viscoelastic models. In the Burger model, the ratio between optimal long-term  $\mu' = \mu_k \mu_e / (\mu_k + \mu_e)$  to the Maxwell shear modulus ( $\mu_e$ ) is close to 2:3 (Ryder *et al.* 2011), thus  $\mu_k$  is fixed at  $6 \times 10^{10}$  Pa. In the standard linear model,  $\mu_k$  is fixed at  $2 \times 10^{10}$  Pa according to Ryder *et al.* (2007). Among these viscoelastic models, the standard linear solid modelling yields the lowest misfit of 2.07 cm with a viscosity of  $3 \times 10^{18}$  Pa s. The misfits of the Maxwell and Burgers body models are 2.23 and 2.16 cm, respectively. The best-fitting parameters for each model and corresponding misfits for the entire time-series are summarized in Table 2.

Fig. 3 shows predicted interferograms for all models. The predicted interferograms of the three models indicate a similar pattern of deformation. The positive lobe widens to east on the southern side of the fault while the negative lobe widens to west on the northern side of the fault. They fit the observed measurement well during the early post-seismic phase. However, the predicted interferograms

indicate that the modelled deformation lobes diffuse farther away and have larger amplitudes at larger distances than the data. This difference increases with time. The deformation lobes shown by InSAR observations are concentrated around the fault, while the model produces notable far-field deformation.

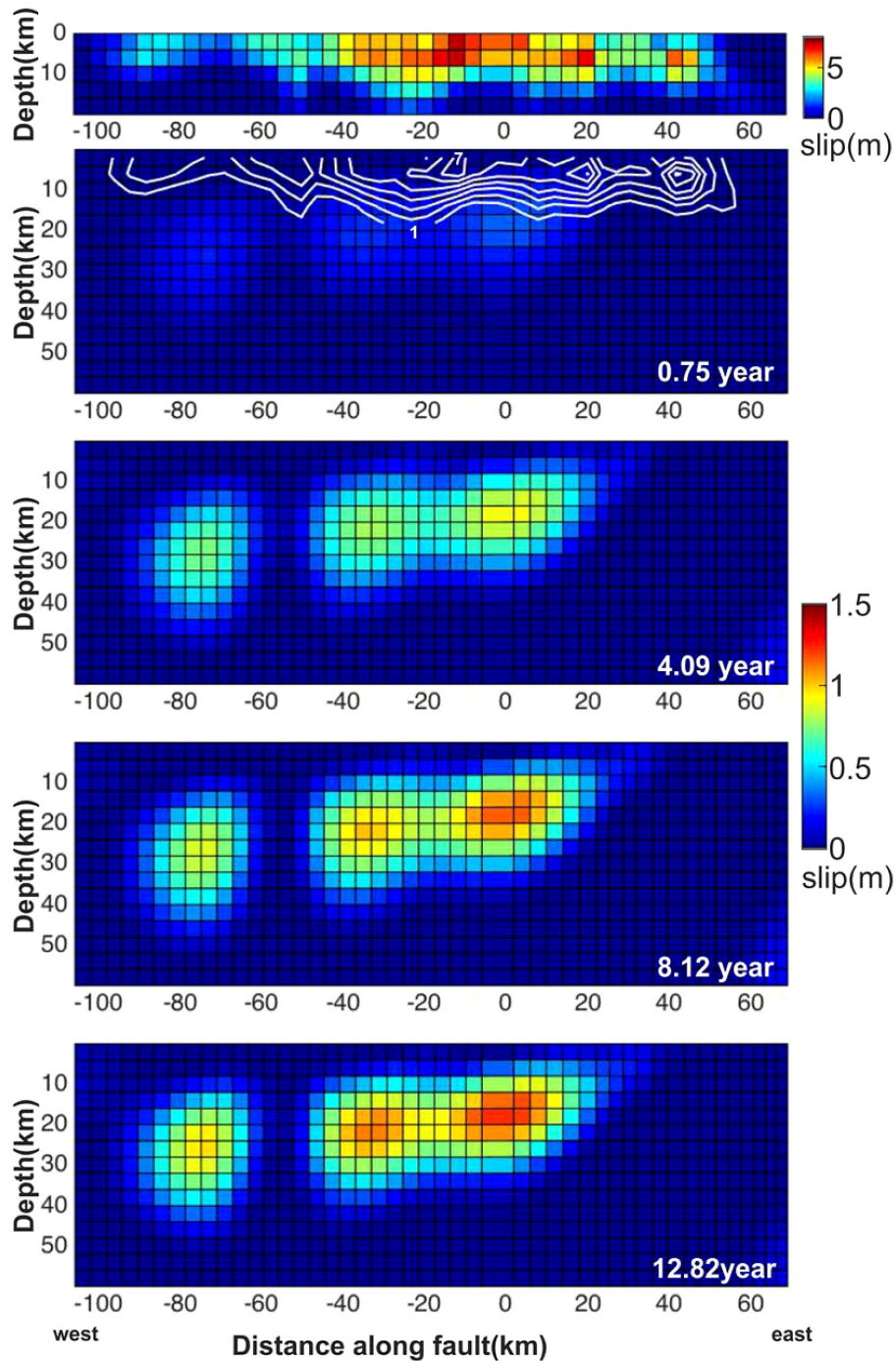
### 3.2 Afterslip modelling

Here we assume that the observed surface deformation is caused by afterslip on the fault plane and its extension. We utilize surface deformation to retrieve slip distribution along the fault plane. The inversion is processed independently at each successive time window such that they are consistent with the time-series data. In our afterslip modelling, the Earth is supposed to be an elastic half-space with no rheological layering. The shear modulus for the half-space is taken as  $\mu = 3.0 \times 10^{10}$  Pa. The fault plane geometry is taken from coseismic interferograms produced by Funning *et al.* (2007). The slip depth is allowed to extend to 60 km during the inversion. The fault plane is discretized into an array of rectangular patches (4 km x 4 km) down-dip resulting in a total of 705 patches. The Green's function approach is employed.  $G$  is a unit model slip, which is estimated by using the Okada formula (Okada 1985). A least-squares algorithm is used for every pixel at successive dates using the following equation (Jónsson *et al.* 2002):

$$\begin{bmatrix} G \\ \kappa^2 \nabla^2 \end{bmatrix} [m] = \begin{bmatrix} d \\ 0 \end{bmatrix}, \quad (2)$$

where  $d$  is the LOS displacement of data,  $m$  is the model solution,  $\nabla^2$  is a second order Laplacian smoothing operator and  $\kappa^2$  is a smoothing factor. The smoothing factor  $\kappa^2$  is determined by looking at the 'knee' of the curve (misfit versus roughness; Jónsson *et al.* 2002). The knee of the curve represents the point of the optimal trade-off between roughness and misfit.

The time-dependent post-seismic slip distributions are shown in Fig. 4. The slip pattern is very stable through time even



**Figure 4.** Post-seismic slip distributions from afterslip inversions. Fault segments are shown as a single plane and view is from the south. The top is the coseismic slip distribution from Funning *et al.* (2007). Post-seismic slip distributions are shown beneath. The contour line shows coseismic slip extraction. The gradient of slip contour is 1 m.

though the amount of slip is increasing over time. The high-slip patches (>0.5 m) concentrate at a depth of 8–40 km, which we will call the creeping segment of the fault. The patches with the highest slip for both coseismic and post-seismic deformation are located along the centre of Manyi fault. The afterslip is located deeper than the coseismic slip. After 12 yr deformation, the maximum afterslip is 1.23 m at a depth of 15~20 km and the moment release is  $\sim 5.96 \times 10^{19}$  N m (equivalent to a sin-

gle event of  $M_w$  7.1), approximately 25 per cent of the coseismic moment.

Predicted interferograms of our afterslip model show a spatially localized deformation pattern, which is very similar to the measured interferograms (Fig. 3). The misfit is  $\sim 1.77$  cm, 15 per cent lower than the viscoelastic models. The residual distribution ranges are smaller relative to viscoelastic models and describe better the spatial deformation pattern farther away from the fault.

## 4 DISCUSSION

### 4.1 Limitations of viscoelastic modelling

To demonstrate the temporal variations in the observed surface displacements, and how well the different models capture rapid decay, the data temporal decay curves are plotted by mean LOS displacements over all pixels on the ground (Fig. 5). The Maxwell model underestimates the displacement which takes place during early phase deformation and gives an overestimation in the later period. Thus, it demonstrates a rather poor fit to the data curves. The Burgers body and standard linear solid capture the features of fast decay better than the Maxwell model. However, the Burgers body model matches the displacement merely in the first several years and standard linear solid model better captures the latter stage of the displacement evolution. It seems, therefore, that the standard linear model can match the temporal behaviour of the overall surface deformation. The key point of the viscoelastic modelling results is that the observed deformation requires two relaxation times, a transient deformation period followed by a steady-state period.

When we look at the spatial pattern of the modelling, we find that viscoelastic modelling cannot reproduce a similar spatial pattern as can be seen in the data. The predicted interferograms of the viscoelastic modelling do not show a localized pattern (Fig. 3). As the distributions diffuse into the far field, the residuals tend to increase (Fig. S1, Supporting Information). To better explore the temporal behaviour of each model, we choose four patches to calculate the mean displacement separately (Fig. 6). The locations of these patches are shown in Fig. S1 of the Supporting Information, where the residual is relatively small for each model (Fig. S1, Supporting Information). The Maxwell model still fits poorly to the data curves. In patches A and B, all viscoelastic models underestimate the deformation. In patch C, the standard linear solid model and Burgers body model are closer to the data but still give underestimations. In patch D, all viscoelastic models overestimate the data displacement. Fig. 7 shows the displacements along an NW–SE profile that crosses the central part of the fault for the above modelling. Displacements are shown for average displacements of pixels within 5 km of the profile line. Viscoelastic models always underestimate displacement along the centre of the fault and overestimate at the far field. They do not reproduce the abrupt transition from the crest to the trough of the data displacement profiles. In addition, their amplitudes are lower and wavelengths are broader when compared to the data. Based on these results, single viscoelastic models are inconsistent with the observed post-seismic deformation obtained from the InSAR data of the Manyi earthquake.

The misfit of the Maxwell modelling is plotted as a function of viscosity (Fig. 8a). This shows that low viscosities are required to explain transient early deformations, while higher viscosities are necessary to explain sustained slow motion. To be able to model the spatio-temporal change of post-seismic deformation, we test a time-dependent viscosity. By assuming an exponential increase in viscosity we reduce the observed difference in each time interval (Fig. 8b). After 20 yr, the viscosity increases to  $5 \times 10^{21}$  Pa s, which reaches the upper bound of the observed range between  $10^{19}$  and  $10^{21}$  Pa s (Hilley *et al.* 2005). We use the viscosities determined by the cumulative deformation (dots in Fig. 8a) to calculate the possibility of time-dependent viscosity model. The misfit reduces from 2.23 cm of uniform viscosity model to 2 cm in the time-dependent viscosity model. Time-dependent viscosity could be a possible explanation for the post-seismic deformation although the misfit reduction of such a time variable model is only 10 per cent.

Such a time-dependent effective viscosity might be a proxy for a power-law rheology. However, the predicted LOS displacement spatial pattern of the power-law mismatch with the data deformation (Fig. S2, Supporting Information), which indicates that the dominant physical mechanism is not likely to be nonlinear deformation. So we do not explore this possibility here.

### 4.2 Applicability of afterslip modelling

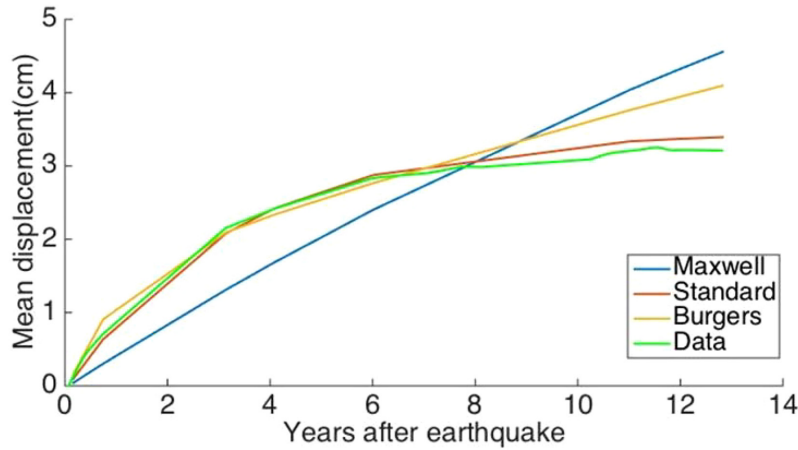
The afterslip model misfit is at least 15 per cent lower than the viscoelastic models and is therefore also lower than the time variable rheology model. The predicted localized spatial pattern of the afterslip model gives more satisfactory reproduction of the data (Fig. 3; Fig. S1, Supporting Information). The temporal shape of the afterslip model better agrees with the data than the viscoelastic models, both for out four patches (Fig. 6) and with regard to the profiles (Fig. 7). We therefore conclude that the afterslip model is consistent with the observed post-seismic deformation.

Taking into account the degrees of freedom, it might not be surprising that the afterslip model performs better than the viscoelastic models as more model parameters are available to describe the complex spatial and temporal behaviour. As a result of this, we test a simplified afterslip model, which contains only the three major patches of the slip area (Fig. S3a, Supporting Information). Also this simplified model can reproduce the localized deformation pattern (Fig. S3b, Supporting Information). The amplitude of the predicted surface deformation is similar to the real data (Fig. S3c, Supporting Information). This test shows that the decrease in misfit of the afterslip model is not attributable to the increase in available model parameter but generally explains better the observed data.

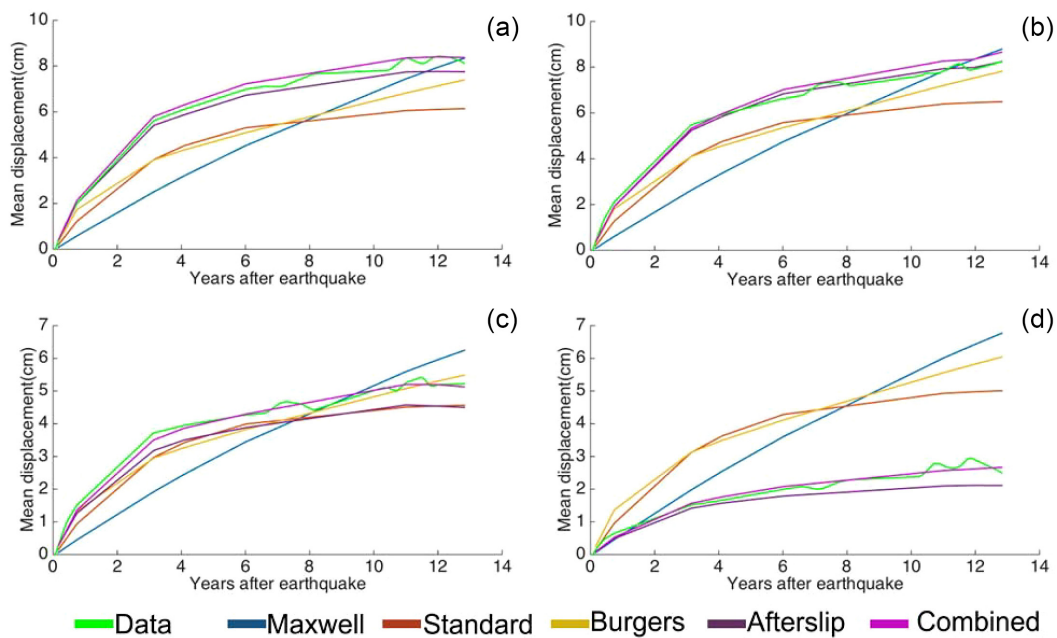
Afterslip has been identified in the decades following an earthquake for several events (e.g. Copley 2014; Copley & Reynolds 2014; Hussain *et al.* 2016). The observed afterslip can last a minimum of 40 yr following the 1964 Alaska earthquake (Suito & Freymueller 2009). Also, afterslip is still taking place from the 1999 Izmit earthquake at an average rate of  $\sim 6$  mm yr<sup>-1</sup> (Cakir *et al.* 2017). These studies suggest that the timescale of afterslip for the Manyi earthquakes is not unique. Ingleby & Wright (2017) suggest that a rate-and-state frictional afterslip model can be consistent with decades of near-field observation results. Therefore, based on our modelling results, as well as residuals and profiles, we inferred that the afterslip model is the single dominant mechanism involved in post-seismic displacements in the near field. However, we cannot rule out the possibility that the more complicated models, such as a combination of viscoelastic and afterslip or nonlinear models, can explain the data and will be explored in the following.

### 4.3 Combined afterslip and viscoelastic modelling

Several studies have shown that combined mechanism models can explain post-seismic displacement by combining afterslip and viscoelastic relaxation (e.g. Biggs *et al.* 2009; Johnson *et al.* 2009). Therefore, we construct a combined model that considers the effects of both afterslip and viscoelastic relaxation. A true joint model should consider the afterslip and viscoelastic relaxation simultaneously and might require less afterslip and more viscoelastic relaxation at deeper depth. Here, we explore the possibility of one end-member scenario, where afterslip dominates post-seismic deformation, and the residual surface deformation can be modelled with viscoelastic relaxation instead of the optimal parameters of these two processes. The elastic and viscoelastic domains have the same elastic properties.



**Figure 5.** Mean displacements against time after the Manyi earthquake. The green line is obtained from the data. The rest curves are obtained from the overall best-fitting parameters of each viscoelastic model. All pixels in the interferogram are taken into account.



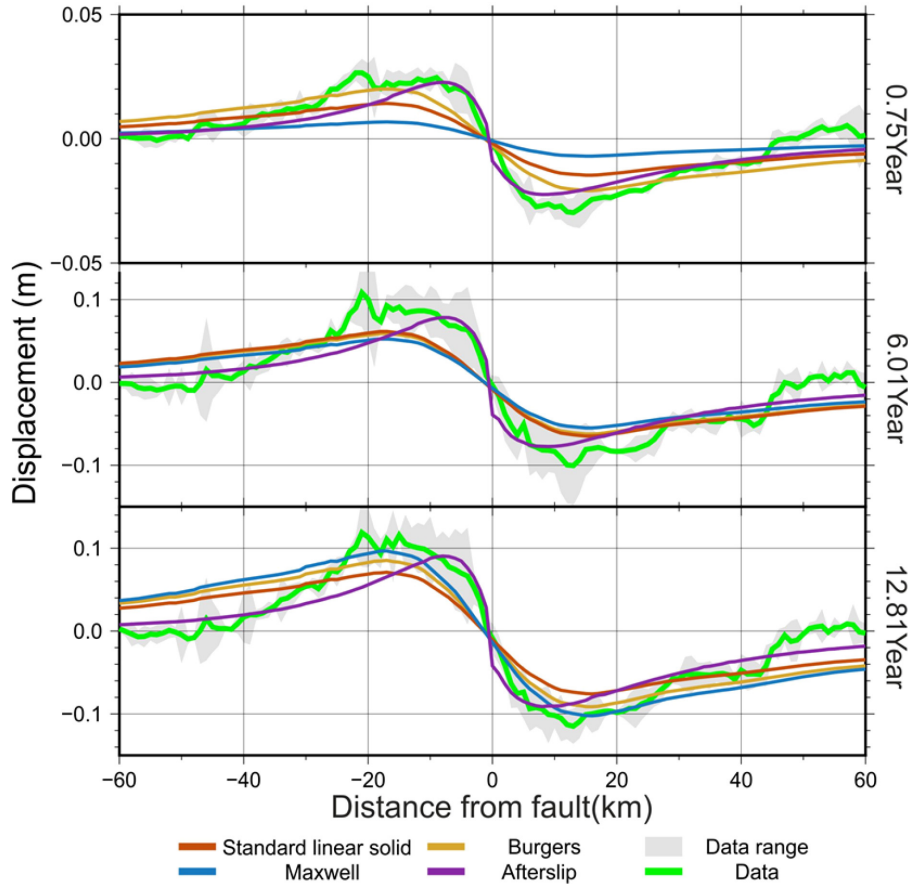
**Figure 6.** Evolution of the mean displacements of patches A, B, C and D, after the Manyi earthquake. The location of each patch is shown in Fig. S1 (Supporting Information). Subplots a, b c and d represent patches A, B, C and D, respectively. The green line is obtained from the data. The rest curves are derived from the overall best-fitting parameters of each viscoelastic model. Combined model has 30 km thick elastic lid over a half-space with viscosity  $5 \times 10^{19}$  Pa s.

As the afterslip can interpret most surface deformation, we take afterslip as the main mechanism. The displacements caused by afterslip are, as in the previous inversion, removed from the LOS displacement. A linear forward viscoelastic modelling below an elastic lid is subsequently calculated using VISCO1D to find any additional viscoelastic relaxation in the crust and mantle (Fig. 9). In these cases, any observed LOS displacements, which are not reproduced by the afterslip model, can be attributed to viscoelastic relaxation (hereafter referred to as residual viscosity). Four values of the thickness of the elastic lid including 15 km (upper crust thickness), 30, 45 km (the middle crustal thickness) and 70 km (the lower crustal thickness) are used. The trade-off curve between misfit and viscosity determines the best-fitting residual viscosity (Fig. S4, Supporting

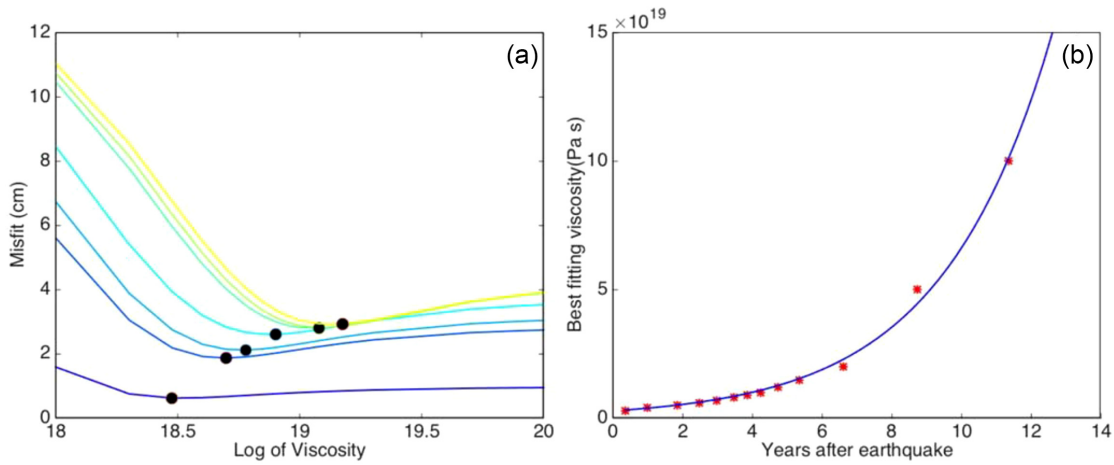
Information). The lower misfits are found for higher viscosity in these cases and  $5 \times 10^{19}$  Pa s is the lower bound of the viscosity. For the residual viscosity of  $5 \times 10^{19}$  Pa s, the corresponding misfits are 1.85, 1.72, 1.77 and 1.76 cm, respectively, for the four different elastic lid thickness model. From the four patches of 30 km elastic lid model (Fig. 6), we can see that each mean displacement has a similar shape to the afterslip model while there is some improvement in fitting the data. The far-field patch D illustrates a great improvement. The viscoelastic mechanism reproduces some far-field deformation in the combined model, which is complementary to afterslip model.

The afterslip and combined mechanism models have similar misfits and reproduce very similar spatial patterns of surface displacements.





**Figure 7.** Swath profile across the fault for each model from early to late time. The width of the profile is 5 km. The profile location is shown in Fig. 3. The grey bar is the range value of the data profile. The bold black line is the average value of the data profile. In the middle picture, the curves of the viscoelastic models almost overlap.

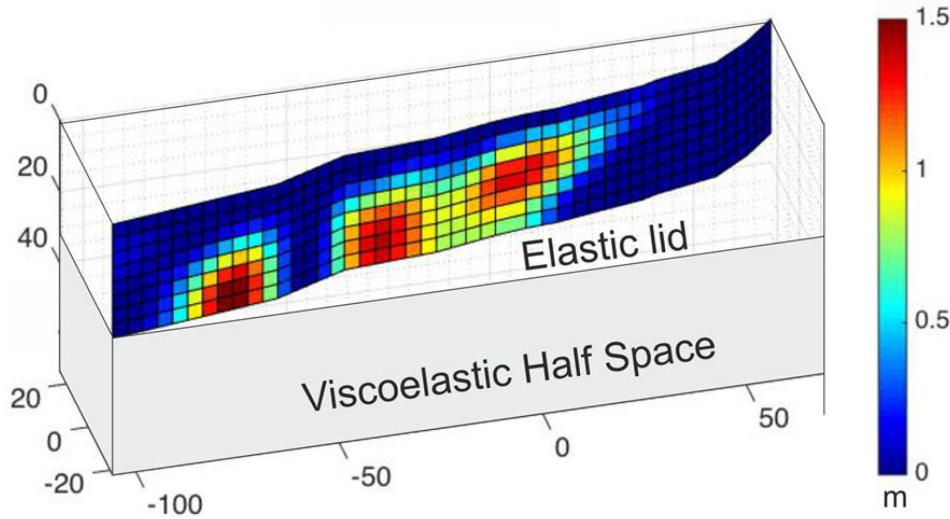


**Figure 8.** (a) Misfit as a function of viscosity. The colour gradient from blue to yellow represents time from early to late. The black dots indicate the minimum misfit. (b) Best-fitting viscosity for each time interval deformation. The red dot represents the viscosity required by the deformation between each time window. The deformation rate between each time interval becomes smaller and smaller over time, which needs larger viscosity to meet the micro change between each time interval.

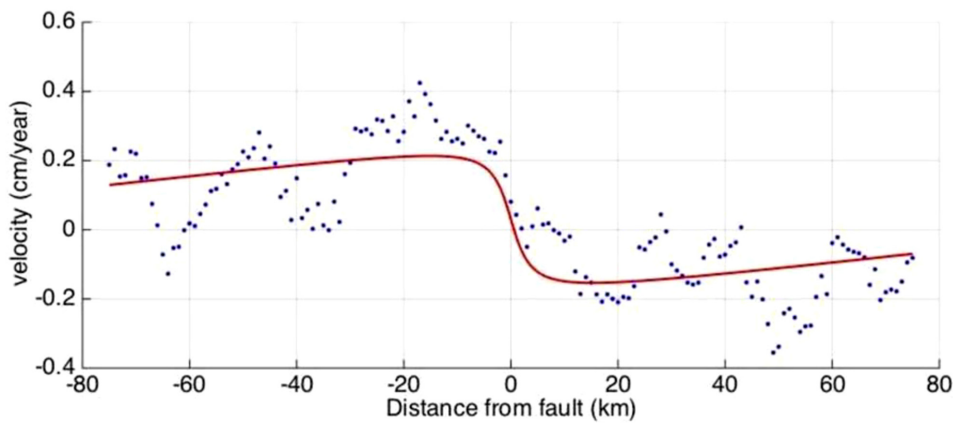
ment. In both mechanisms, the afterslip process reproduces the largest part of the surface deformation. The viscoelastic relaxation slightly improves the fit to the data especially at larger distances from the fault. Therefore, a combination of afterslip and viscoelastic relaxation is also a feasible process.

#### 4.4 Rate of late post-seismic deformation

To further explore post-seismic deformation, we stacked interferograms from 2008 to 2010. This method adds  $N$  independent interferograms together and averaging them to reduce the spatially uncorrelated noise by  $1/\sqrt{N}$  (Biggs *et al.* 2007). This method has been used



**Figure 9.** The sketch map of combined mechanism model. The viscoelastic relaxation has an elastic layer thickness of 30 km over a half-space with viscosity  $5 \times 10^{19}$  Pa s.



**Figure 10.** Profile across the InSAR LOS rate map. Averaged LOS rate (vertical axis) is plotted against the distance (horizontal axis) from the fault. The profile location is the same as shown in Fig. 3. Point measurements are taken within the 10-km-wide band along the profile. The red line represents the best-fitting curve for the data.

to calculate interseismic strain accumulation in many places, e.g. Turkey (Wright *et al.* 2001), California (Lyons & Sandwell 2003) and Tibet (Wright *et al.* 2004). From the stack, we can see that the Manyi fault is still moving, at a maximum motion rate of  $\sim 5$  mm  $\text{yr}^{-1}$  near the fault zone. To illustrate the rate map more clearly, we extracted a swath profile across the central fault (Fig. 10). Average LOS velocities inferred from the central profile of the stacked InSAR data give an initial impression of a change in velocity. The average velocity close to the fault is  $\sim 4$  mm  $\text{yr}^{-1}$ , twice the far-field velocity. Bell *et al.* (2011) calculated the interseismic motion rate of the Manyi fault to be  $3 \pm 2$ , and 1 mm  $\text{yr}^{-1}$  just prior to the earthquake. Our LOS velocities almost reach the upper bound of the interseismic motion rate. The LOS velocity profile appears to approximate an arctangent sigmoid trend although the velocity does not increase with distance from the fault. Through the alluvial terrace that was formed after the Holocene, horizontal sinistral slip on the Manyi fault is at a rate of 4 mm  $\text{yr}^{-1}$  (Xu 2000). This result (4 mm  $\text{yr}^{-1}$ ) is consistent with the InSAR result ( $3 \pm 2$  mm  $\text{yr}^{-1}$ ) from Bell *et al.* (2011). For our current InSAR data set, these studies suggest that the post-seismic deformation of the Manyi earthquake might be vanishing and gradually stepping into an interseismic phase.

There is a progressive increase of left lateral slip from the northwest to the southeast along the Xianshuihe–Ganzi–Yushu fault zone (Wang *et al.* 2008; Wang *et al.* 2013). The slip rate of the Fenghuoshan fault, the northwestern segment of this fault zone, is about  $6.1 \pm 1.9$  mm  $\text{yr}^{-1}$ . Our observations support a decay in slip rate towards the western end of the Xianshuihe–Ganzi–Yushu fault zone, if the latest 3 yr (2008–2010) of post-seismic deformation rate represents the interseismic rate.

### 5 CONCLUSION

Following the 1997  $M_w$  7.6 Manyi earthquake, InSAR analysis provides insight into the relatively long timescale of post-seismic deformation. We have investigated four possible mechanisms: the Maxwell, standard linear solid, Burgers body viscoelastic models and the afterslip model. All the viscoelastic models are constructed using an elastic layer overlying the uniform viscoelastic properties. The Maxwell model (misfit = 2.23 cm) does not fit the data and although the standard linear solid (misfit = 2.07 cm) and Burgers body (misfit = 2.16 cm) models have two relaxation times, they cannot match the observed temporal–spatial deformation patterns.

For the mean deformation over all pixels they have a good temporal reproduction, but for the spatial distribution they cannot fit the data. Additionally, a time-dependent viscosity model reduces the misfit to 2 cm, which provides a possible explanation for the deformation. The afterslip model has the smallest misfit of 1.77 cm and can better match the spatio-temporal behaviour of the surface deformation. The maximum afterslip is 1.23 m 12 yr after the earthquake. We also explored the possibility of combined mechanisms where both afterslip and viscoelastic relaxation contribute to the post-seismic deformation. For this case the misfit (1.72 cm) slightly decreases. Our LOS velocity between 2008 and 2010 is  $\sim 4 \text{ mm yr}^{-1}$ , which almost reaches the upper bound of the interseismic motion rate. Therefore, the post-seismic deformation might gradually step into an interseismic phase.

## 5.1 Data

Time-series data (data used in eq. 1) are available in the Supporting Information.

## ACKNOWLEDGEMENTS

MF was supported by the Chinese scholarship council (CSC). I would like to thank James Holt for helping me improve the language of the manuscript. All ERS and Envisat data were obtained from the European Space Agency. We thank two anonymous reviewers and the Editor Prof. Duncan Agnew for their valuable comments.

## REFERENCES

- Bell, M.A., Elliott, J.R. & Parsons, B.E., 2011. Interseismic strain accumulation across the Manyi fault (Tibet) prior to the 1997  $M_w$  7.6 earthquake, *Geophys. Res. Lett.*, **38**.
- Berardino, P., Fornaro, G., Lanari, R. & Sansosti, E., 2002. A new algorithm for surface deformation monitoring based on small baseline differential SAR interferograms, *IEEE Trans. Geosci. Remote Sensing*, **40**, 2375–2383.
- Biggs, J., Wright, T., Lu, Z. & Parsons, B., 2007. Multi-interferogram method for measuring interseismic deformation: Denali Fault, Alaska, *Geophys. J. Int.*, **170**, 1165–1179.
- Biggs, J., Bürgmann, R., Freymueller, J.T., Lu, Z., Parsons, B., Ryder, I., Schmalzle, G. & Wright, T., 2009. The postseismic response to the 2002  $M$  7.9 Denali Fault earthquake: constraints from InSAR 2003–2005, *Geophys. J. Int.*, **176**, 353–367.
- Bürgmann, R., Ergintav, S., Segall, P., Hearn, E.H., McClusky, S., Reilinger, R.E., Woith, H. & Zschau, J., 2002. Time-dependent distributed afterslip on and deep below the Izmit earthquake rupture, *Bull. seism. Soc. Am.*, **92**, 126–137.
- Cakir, Z., Aslan, G., Cetin, S., Dogan, U., Ergintav, S., Lasserre, C., Renard, F. & Reilinger, R., 2017. Postseismic deformation of the 1999 Izmit Earthquake (Turkey)-the longest recorded afterslip on a major continental fault, in AGU Fall Meeting Abstracts, New Orleans, Abstract no. #T13E-01.
- Cavalié, O., Doin, M.P., Lasserre, C. & Briole, P., 2007. Ground motion measurement in the Lake Mead area, Nevada, by differential synthetic aperture radar interferometry time series analysis: probing the lithosphere rheological structure, *J. geophys. Res.*, **112**.
- Copley, A., 2014. Postseismic afterslip 30 years after the 1978 Tabas-e-Golshan (Iran) earthquake: observations and implications for the geological evolution of thrust belts, *Geophys. J. Int.*, **197**, 665–679.
- Copley, A. & Reynolds, K., 2014. Imaging topographic growth by long-lived postseismic afterslip at Sefidabeh, east Iran, *Tectonics*, **33**, 330–345.
- Dziewoński, A., Chou, T.A. & Woodhouse, J., 1981. Determination of earthquake source parameters from waveform data for studies of global and regional seismicity, *J. geophys. Res.*, **86**, 2825–2852.
- Ekström, G., Nettles, M. & Dziewoński, A., 2012. The global CMT project 2004–2010: centroid-moment tensors for 13,017 earthquakes, *Phys. Earth planet. Inter.*, **200**, 1–9.
- Farr, T.G., et al., 2007. The shuttle radar topography mission, *Rev. Geophys.*, **45**.
- Fialko, Y., 2004. Evidence of fluid-filled upper crust from observations of postseismic deformation due to the 1992  $M_w$  7.3 Landers earthquake, *J. geophys. Res.*, **109**.
- Freed, A.M., 2007. Afterslip (and only afterslip) following the 2004 Parkfield, California, earthquake, *Geophys. Res. Lett.*, **34**.
- Funning, G.J., Parsons, B. & Wright, T.J., 2007. Fault slip in the 1997 Manyi, Tibet earthquake from linear elastic modelling of InSAR displacements, *Geophys. J. Int.*, **169**, 988–1008.
- Hetland, E.A. & Zhang, G., 2014. Effect of shear zones on post-seismic deformation with application to the 1997  $M_w$  7.6 Manyi earthquake, *Geophys. J. Int.*, **198**, 259–269.
- Hilley, G.E., Bürgmann, R., Zhang, P.Z. & Molnar, P., 2005. Bayesian inference of plastosphere viscosities near the Kunlun Fault, northern Tibet, *Geophys. Res. Lett.*, **32**.
- Hussain, E., Wright, T.J., Walters, R.J., Bekaert, D., Hooper, A. & Houseman, G.A., 2016. Geodetic observations of postseismic creep in the decade after the 1999 Izmit earthquake, Turkey: implications for a shallow slip deficit, *J. geophys. Res.*, **121**, 2980–3001.
- Ingleby, T. & Wright, T., 2017. Omori-like decay of postseismic velocities following continental earthquakes, *Geophys. Res. Lett.*, **44**, 3119–3130.
- Jiang, M., Galvé, A., Hirn, A., De Voogd, B., Laigle, M., Su, H., Diaz, J., Lépine, J.-C. & Wang, Y., 2006. Crustal thickening and variations in architecture from the Qaidam basin to the Qang Tang (North–Central Tibetan Plateau) from wide-angle reflection seismology, *Tectonophysics*, **412**, 121–140.
- Johnson, K.M., Bürgmann, R. & Freymueller, J.T., 2009. Coupled afterslip and viscoelastic flow following the 2002 Denali Fault, Alaska earthquake, *Geophys. J. Int.*, **176**, 670–682.
- Jónsson, S., Zebker, H., Segall, P. & Amelung, F., 2002. Fault slip distribution of the 1999  $M_w$  7.1 Hector Mine, California, earthquake, estimated from satellite radar and GPS measurements, *Bull. seism. Soc. Am.*, **92**, 1377–1389.
- Jonsson, S., Segall, P., Pedersen, R. & Björnsson, G., 2003. Post-earthquake ground movements correlated to pore-pressure transients, *Nature*, **424**, 179–183.
- Lyons, S. & Sandwell, D., 2003. Fault creep along the southern San Andreas from interferometric synthetic aperture radar, permanent scatterers, and stacking, *J. geophys. Res.*, **108**.
- Nishimura, T. & Thatcher, W., 2003. Rheology of the lithosphere inferred from postseismic uplift following the 1959 Hebgen Lake earthquake, *J. geophys. Res.*, **108**.
- Okada, Y., 1985. Surface deformation due to shear and tensile faults in a half-space, *Bull. seism. Soc. Am.*, **75**, 1135–1154.
- Peltzer, G., Crampe, F. & King, G., 1999. Evidence of nonlinear elasticity of the crust from the  $M_w$  7.6 Manyi (Tibet) earthquake, *Science*, **286**, 272–276.
- Pollitz, F.F., 1997. Gravitational viscoelastic postseismic relaxation on a layered spherical Earth, *J. geophys. Res.*, **102**, 17 921–17 941.
- Pollitz, F.F., 2005. Transient rheology of the upper mantle beneath central Alaska inferred from the crustal velocity field following the 2002 Denali earthquake, *J. geophys. Res.*, **110**.
- Pollitz, F.F., Peltzer, G. & Bürgmann, R., 2000. Mobility of continental mantle: Evidence from postseismic geodetic observations following the 1992 Landers earthquake, *J. geophys. Res.*, **105**, 8035–8054.
- Qidong, D., Xiang, G. & Guihua, C., 2010. Recent tectonic activity of Bayankala fault-block and the Kunlun-Wenchuan earthquake series of the Tibetan Plateau, *Earth Sci. Frontiers*, **17**, 163–178.
- Rosen, P.A., Hensley, S., Peltzer, G. & Simons, M., 2004. Updated repeat orbit interferometry package released, *EOS, Trans. Am. Geophys. Un.*, **85**, 47–47.
- Ryder, I., Parsons, B., Wright, T.J. & Funning, G.J., 2007. Post-seismic motion following the 1997 Manyi (Tibet) earthquake: InSAR observations and modelling, *Geophys. J. Int.*, **169**, 1009–1027.

Ryder, I., Bürgmann, R. & Pollitz, F., 2011. Lower crustal relaxation beneath the Tibetan Plateau and Qaidam Basin following the 2001 Kokoxili earthquake, *Geophys. J. Int.*, **187**, 613–630.

Ryder, I., Wang, H., Bie, L. & Rietbrock, A., 2014. Geodetic imaging of late postseismic lower crustal flow in Tibet, *Earth planet. Sci. Lett.*, **404**, 136–143.

Schmidt, D.A. & Bürgmann, R., 2003. Time-dependent land uplift and subsidence in the Santa Clara valley, California, from a large interferometric synthetic aperture radar data set, *J. geophys. Res.*, **108**.

Suito, H. & Freymueller, J.T., 2009. A viscoelastic and afterslip postseismic deformation model for the 1964 Alaska earthquake, *J. geophys. Res.*, **114**.

Wang, S., Fan, C., Wang, G. & Wang, E., 2008. Late Cenozoic deformation along the northwestern continuation of the Xianshuihe fault system, Eastern Tibetan Plateau, *Bull. geol. Soc. Am.*, **120**, 312–327.

Wang, Y., Wang, M., Shen, Z.-K., Ge, W., Wang, K., Wang, F. & Sun, J., 2013. Inter-seismic deformation field of the Ganzi-Yushu fault before the 2010  $M_w$  6.9 Yushu earthquake, *Tectonophysics*, **584**, 138–143.

Wen, Y., Li, Z., Xu, C., Ryder, I. & Bürgmann, R., 2012. Postseismic motion after the 2001  $M_w$  7.8 Kokoxili earthquake in Tibet observed by InSAR time series, *J. geophys. Res.*, **117**.

Wright, T., Parsons, B. & Fielding, E., 2001. Measurement of interseismic strain accumulation across the North Anatolian Fault by satellite radar interferometry, *Geophys. Res. Lett.*, **28**, 2117–2120.

Wright, T.J., Parsons, B., England, P.C. & Fielding, E.J., 2004. InSAR observations of low slip rates on the major faults of western Tibet, *Science*, **305**, 236–239.

Wright, T.J., Elliott, J.R., Wang, H. & Ryder, I., 2013. Earthquake cycle deformation and the Moho: implications for the rheology of continental lithosphere, *Tectonophysics*, **609**, 504–523.

Xu, X., 2000. Scientific survey for the Manyi earthquake, *China Earthquake Yearbook*, Seismological Press, pp. 327–329.

Yamasaki, T. & Houseman, G.A., 2012. The crustal viscosity gradient measured from post-seismic deformation: a case study of the 1997 Manyi (Tibet) earthquake, *Earth planet. Sci. Lett.*, **351**, 105–114.

Zhao, W. *et al.*, 2001. Crustal structure of central Tibet as derived from project INDEPTH wide-angle seismic data, *Geophys. J. Int.*, **145**, 486–498.

Pollitz, F.F., 2015. Postearthquake relaxation evidence for laterally variable viscoelastic structure and water content in the Southern California mantle, *Journal of Geophysical Research: Solid Earth*, **120**(4), 2672–2696.

SUPPORTING INFORMATION

Supplementary data are available at *GJI* online.

**Figure S1.** Residuals for each model from early to late time period (calculated as the model minus data). Here, only four dates are presented to show the residual change tendency. The black squares show the location of Patches A, B, C and D. The mean displacements of these patches are used in the discussion to explore the temporal behaviour of each model.

**Figure S2.** Range change predicted by nonlinear model at 11th yr after the earthquake. The spatial deformation pattern bears little similarity to that of the time-series (Fig. 3). Red line marks position of fault.

**Figure S3.** The three patches afterslip model inversion results. (a) The slip distributions from three patch afterslip inversions after 12 yr of earthquake. (b) Predicted surface deformation by this simplified model. (c) Corresponding residual.

**Figure S4.** Trade-off curve between residual viscosity of viscoelastic model and misfit of the combined model. The thickness of elastic lid is 30 km. The viscosity is  $5 \times 10^{19}$  Pa s of the red point, which model sketch map and displacement shows in Figs 6 and 9.

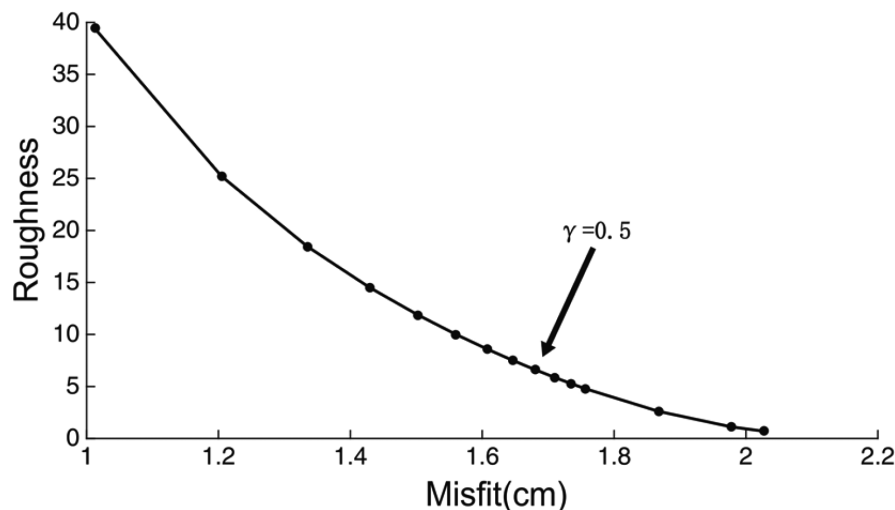
Please note: Oxford University Press is not responsible for the content or functionality of any supporting materials supplied by the authors. Any queries (other than missing material) should be directed to the corresponding author for the article.

APPENDIX A: TIME-SERIES CONSTRUCTION

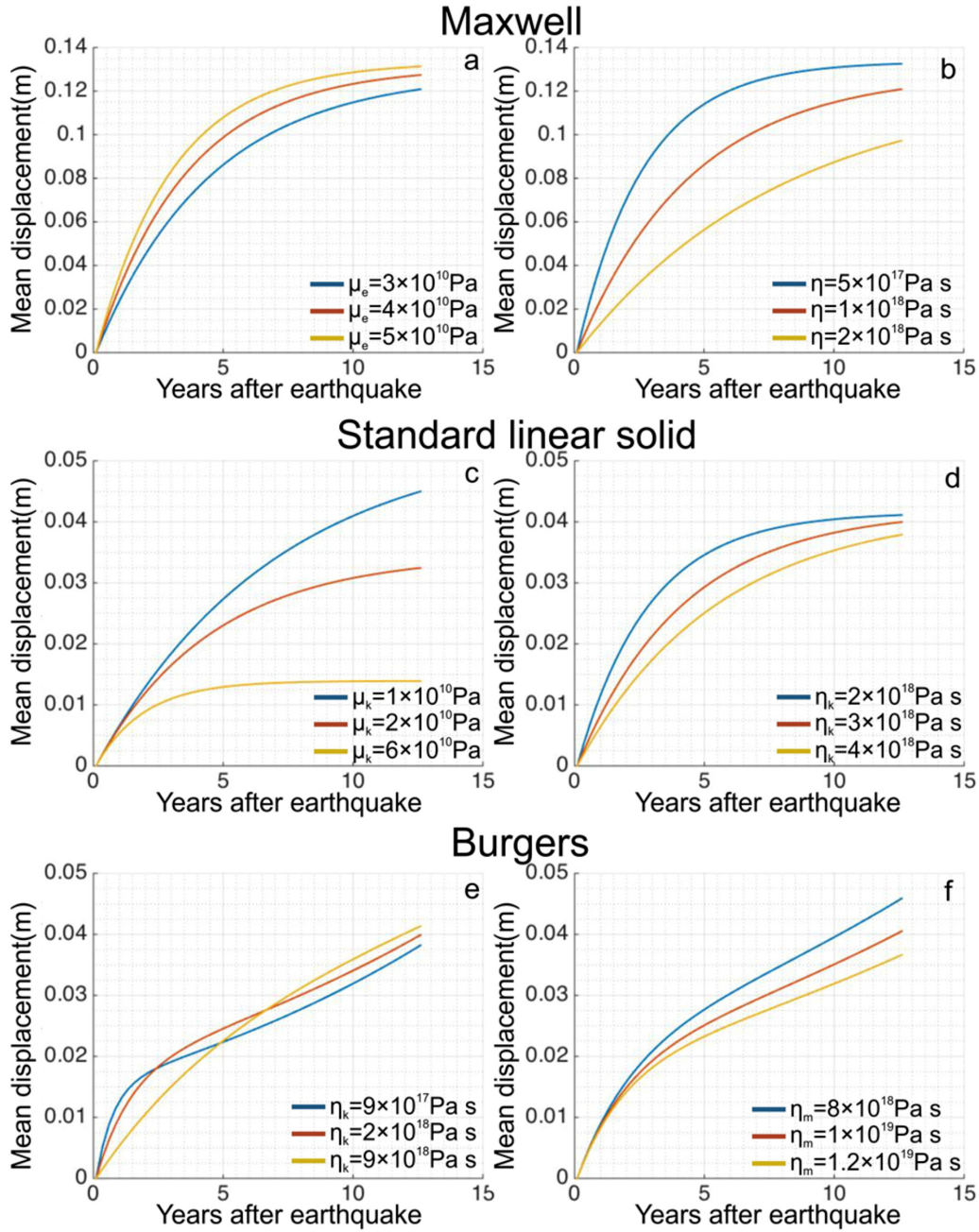
A set of  $N$  interferograms are constructed using  $S$  independent SAR acquisitions. Let  $\mathbf{t}$  be the vector of SAR acquisitions ordered by date. For a given interferogram, the data range between the start time  $t_k$  and end time  $t_{k+1}$ :  $m_{ab}$  can be written as

$$m_{ab} = \sum_{k=a}^{b-1} v_{k,k+1} (t_{k+1} - t_k), \tag{A1}$$

where the index  $k$  is the serial number of the date in acquisition matrix  $t$ , and  $v_{k,k+1}$  is the velocity between time  $t_k$  and  $t_{k+1}$ . The



**Figure A1.** Roughness plotted against misfit for different smoothing factors in the time-series matrix. The point marks the smoothing factor ( $\gamma$ ) of 0.5, which is used in this study.



**Figure A2.** Mean displacements predicted by different viscoelastic models with various rheological model parameters. (a) Maxwell model,  $\eta = 10^{18}$  Pa s, varying  $\mu_e$ . (b) Maxwell model,  $\mu_e = 3 \times 10^{10}$  Pa, varying  $\eta$ . (c) Standard linear solid model,  $\mu_e = 3 \times 10^{10}$  Pa,  $\eta_k = 4 \times 10^{18}$  Pa s, varying  $\mu_k$ . (d) Standard linear solid model,  $\mu_e = 3 \times 10^{10}$  Pa,  $\mu_k = 1.5 \times 10^{10}$  Pa, varying  $\eta_k$ . (e) Burgers body model,  $\mu_e = 3 \times 10^{10}$  Pa,  $\mu_k = 6 \times 10^{10}$  Pa,  $\eta_m = 1 \times 10^{19}$  Pa s, varying  $\eta_k$ . (f) Burgers body model,  $\mu_e = 3 \times 10^{10}$  Pa,  $\mu_k = 6 \times 10^{10}$  Pa,  $\eta_k = 3 \times 10^{18}$  Pa s, varying  $\eta_m$ .

date immediately following the earthquake is taken as the reference time for all interferograms. This ensures that all deformation is measured relative to a common date. We calculate the range change by summing up the incremental range changes from preceding time steps. The entire data set can be written as follows:

$$Tv = r, \quad (\text{A2})$$

where  $T$  is an  $N \times (S - 1)$  matrix of time reference interval,  $v$  is an  $(S - 1) \times 1$  vector of successive velocities between two adjacent acquisitions and  $r$  is a vector containing displacement measurements. To avoid significant discontinuities we used velocity instead of displacement during the inversion (Berardino *et al.* 2002).

A smoothing constraint was used to reduce the effect of atmospheric noise. It assumes that less deformation occurs over short time intervals. The smoothing constraint is written as

$$T^s v = 0, \quad (\text{A3})$$

where  $0$  is an  $(S - 2)$  column vector of zeros.  $T^s$  is an  $(S - 2)$  by  $(S - 1)$  matrix which has the following form:

$$\begin{cases} T_{j,j}^s = -1 \\ T_{j,j+1}^s = +1 \end{cases} \quad (\text{A4})$$

Temporal velocity evolution is obtained by solving the following equation:

$$\begin{bmatrix} T \\ \gamma T^s \end{bmatrix} [v] = \begin{bmatrix} r \\ 0 \end{bmatrix} \quad (\text{A5})$$

If the smoothing factor  $\gamma$  is too large, the deformation signal will be overdamped. On the other hand, if the smoothing factor  $\gamma$  is too small, there will be significant fluctuation from time step to time step. We chose the optimal smoothing factor by considering the trade-off between model fit (misfit) and model roughness. Choosing a value at the ‘knee’ of the curve for the smoothing factor we obtain  $\gamma = 0.5$  (Fig. A1). Adjacent values of the smoothing factor do not show significant differences in the constructed time-series result.

Once we have velocities from the least-squares solution, the overall displacement was calculated from the successive velocities. For the very early phase, namely the first month, transient deformation is approximately linear (Ryder *et al.* 2007), so the velocity can be extrapolated to the time of the earthquake itself.

## APPENDIX B: MODEL SET-UP

The Maxwell analogue is composed of a spring with shear modulus  $\mu_e$  and a viscous damper with viscosity  $\eta$  in series and has a single relaxation time  $\tau = \frac{\eta}{\mu_e}$ . If we keep the viscosity ( $\eta$ ) fixed and vary the shear modulus ( $\mu_e$ ), the relaxation time ( $\tau$ ) will decrease as shear modulus increase (Fig. A2a). While increasing the half-space viscosity ( $\eta$ ) and keeping the shear modulus ( $\mu_e$ ) at constant, the relaxation time ( $\tau$ ) of the transient process will also increase (Fig. A2b). In our study, the elastic modulus  $\mu_e$  is assumed at  $3 \times 10^{10}$  Pa (in line with previous studies) and the viscosity is taken in the range of  $10^{18}$ – $10^{20}$  Pa s.

The standard linear solid model is conceptually composed of a Kelvin element in series with a spring with shear modulus  $\mu_e$ . The Kelvin element consists of an elastic component with shear modulus  $\mu_k$  in parallel with a viscous component with viscosity  $\eta_k$ . It is the simplest element that can describe both delayed elasticity and stress relaxation. The system is initially governed by shear modulus  $\mu_e$ , and then falls to long-term shear modulus  $\mu' = \mu_k \mu_e / (\mu_k + \mu_e)$  as stress relax. Keeping the viscosity ( $\eta_k$ ) and shear modulus ( $\mu_e$ )

fixed, we find that both displacement magnitude and the time of the transient will increase with the decrease of shear modulus ( $\mu_k$ ) of Kelvin element (Fig. A2c). At the end of relaxation, there is a single governing shear modulus  $\mu'$ . If we keep both shear modulus at constant and vary the viscosity, we can find that relaxation time will increase according to  $\tau = \frac{\eta}{\mu'}$  (Fig. A2d). In the study we keep the shear modulus  $\mu_e$  constant at  $3 \times 10^{10}$  Pa, the same as the Maxwell model. The viscosity  $\eta_k$  is taken in the range of  $10^{18}$ – $10^{20}$  Pa s and shear modulus of Kelvin element  $\mu_k$  is varied between  $1 \times 10^{10}$  and  $6 \times 10^{10}$  Pa.

The Burgers body model is represented by a Kelvin element in series with a Maxwell element. This configuration has two relaxation times due to two viscous components. The standard linear solid model is an extreme case of the Burgers body model when the Maxwell viscosity ( $\eta_m$ ) becomes infinite. Similarly, if the viscosity of the Kelvin element ( $\eta_k$ ) becomes infinite, then the material will behave as a Maxwell body. During the transient relaxation period, the shear modulus relaxes from  $\mu_e$  to long-term shear modulus  $\mu' = \mu_k \mu_e / (\mu_k + \mu_e)$ . We still fix the shear modulus  $\mu_e$  at  $3 \times 10^{10}$  Pa for comparison purposes. Ryder *et al.* 2011 suggested the optimal ratio for long-term shear modulus to Maxwell shear modulus is 2:3, thus  $\mu_k$  will be fixed at  $6 \times 10^{10}$  Pa. If we keep the Maxwell viscosity ( $\eta_m$ ) constant, it follows that the weaker the Kelvin element is, the larger the difference between the two timescales will be. The two phases of post-seismic relaxation differ significantly, which can be seen through curve gradient (Fig. A2e). The steady-state viscosity  $\eta_m$  controls the magnitude of displacement because the Burgers body model is more sensitive to Maxwell viscosity (Ryder *et al.* 2011). The fully relaxed displacements do not have much variation as they have same  $\eta_m$ . However, if we keep  $\eta_k$  constant and increase  $\eta_m$ , the behaviour of transient state process of those models are the same since they have same Kelvin viscosity (Fig. A2f). In the following steady-state relaxation, the displacement magnitude decreases with the increasing Maxwell viscosity ( $\eta_m$ ). The larger the  $\eta_m$  is, the slower the displacement will increase with time. The  $\eta_m$  range will be taken between  $10^{18}$  and  $10^{20}$  Pas and  $\eta_k$  will be taken between  $10^{17}$  and  $10^{19}$  Pas in the modelling. When the steady viscosity increase to  $1 \times 10^{21}$  Pa s or larger, the Burger modelling result performs nearly equal to the standard linear result.